Environmental Science & Technology

pubs.acs.org/est

Article

Thermodynamic and Kinetic Analyses of Ion Intercalation/Deintercalation Using Different Temperatures on NiHCF Electrodes for Battery Electrode Deionization

Le Shi, Xiangyu Bi, Evan Newcomer, Derek M. Hall, Christopher A. Gorski, and Bruce E. Logan*

Cite This: *Environ. Sci. Technol.* 2022, 56, 8932−8941

Read Online

ACCESS | Metrics & More | Article Recommendations | Supporting Information

ABSTRACT: Prussian blue analogues are used in electrochemical deionization due to their cation sorption capabilities and ion selectivity properties. Elucidating the fundamental mechanisms underlying intercalation/deintercalation is important for the development of ion-selective electrodes. We examined the thermodynamic and kinetic properties of nickel hexacyanoferrate electrodes by studying different temperatures effects on intercalation/deintercalation with monovalent ions (Li^+, Na^+, K^+, and NH_4^+) relevant to battery electrode deionization applications. Higher temperatures reduced the interfacial charge transfer resistance and increased the diffusion coefficient of cations in the solid material. Ion transport in the solid material, rather than interfacial charge transfer, was found to be the rate-controlling step, as shown by higher activation energies for ion transport (e.g., 31 ± 3 kJ/mol for K^+) than for interfacial charge transfer (5 ± 1 kJ/mol for K^+). The largest increase in cation adsorption capacity with temperature was observed for NH_4^+ (28.1% from 15 to 75 °C) due to its smallest activation energy. These results indicate that ion hydration energy determines the intercalation potential and activation energies of ion transport in solid material control intercalation/deintercalation rate. Together with the endothermic behavior of deintercalation and exothermic behavior of intercalation, the higher operating temperature results in improvement of ion adsorption capacity depending on specific cations.

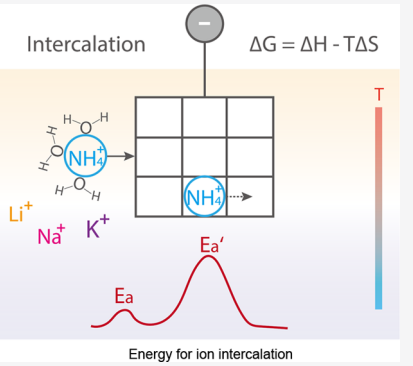

KEYWORDS: *electrochemical deionization, Prussian blue analogues, charge transfer activation energy, ion transport activation energy, thermodynamic and kinetic properties*

Downloaded via PENNSYLVANIA STATE UNIV on August 7, 2022 at 12:50:04 (UTC).
See https://pubs.acs.org/sharingguidelines for options on how to legitimately share published articles.

INTRODUCTION

Electrochemical deionization technologies, such as capacitive deionization (CDI) and battery deionization (BDI), have been examined for deionization and nutrient recovery applications due to their good performance in selective removal of ions with low energy consumption and high thermodynamic energy efficiencies.[1−6] In CDI, ions are stored in the electrical double layer (EDL) on the surfaces of capacitive electrodes byan electric field.[7] In BDI using battery-type electrodes, for example, Prussian blue analogues (PBA), cations are intercalated into the crystal structures of PBA by faradaic processes with optima at certain electrode potentials.[5,8−10] The performance of both CDI and BDI systems can be impacted by various operating conditions, such as charge−discharge modes,[11] charge−discharge rates,[5] feed solution flow rate,[12] feed solution concentrations,[13] and solution pH.[14] However, the thermodynamic and kinetic properties of cation intercalation/deintercalation for PBA electrodes used in BDI applications are relatively unexplored. One way to examine these properties is to test their electrochemical performance as a function of temperature. However, most BDI studies have only been conducted at room temperature.

The effect of temperature on ion sorption performance has been examined in capacitive electrochemical deionization systems such as CDI and membrane CDI (MCDI), and energy storage devices such as supercapacitors, but not in BDI. Using MCDI, it was found that increasing a feed solution temperature from 20 to 50 °C reduced the electrical energy consumed for a 0.5 M NaCl solution by nearly 10%.[15] In another CDI study using 20 mM NaCl, variable-temperature profiles of feed solution were shown to affect thermodynamic efficiencies by altering the ion structuring and extension charge storage dynamics within the electric double layer (EDL).[16] Higher temperatures (45 vs 15 °C) have been found in CDI tests to enhance Na^+ adsorption and desorption rates but reduce the adsorption capacity of Na^+.[17] In contrast, there was an improvement in adsorption capacity with increasing temperature of the electrode (from −20 to 60 °C) using porous activated carbon electrodes with an ionic liquid electrolyte.[18] Similarly, for a pseudocapacitor (PEDOT:PSS-

Received: March 4, 2022
Revised: May 15, 2022
Accepted: May 19, 2022
Published: June 8, 2022

© 2022 American Chemical Society

https://doi.org/10.1021/acs.est.2c01586
Environ. Sci. Technol. 2022, 56, 8932−8941

coated graphene electrode), the capacity increased by ~1.5 times, compared to 3.7 times for a capacitor (graphene electrode) with an increase in the temperature from room temperature to ~39 °C.[19] Heating the electrode also improved the Li^+ adsorption capacity in a supercapacitor with a hybrid nickel-based PBA/NiO nanotube electrode.[20] These studies have therefore shown trade-offs in rates and extents of electrode storage capacities at elevated temperatures either by heating the solution or by heating the electrodes, but tests have not been conducted under conditions directly relevant for deionization using PBA electrodes.

In this study, we examined the thermodynamic and kinetic properties of the intercalation/ deintercalation process for several monovalent ions (Li^+, Na^+, K^+, and NH_4^+) relevant for BDI applications, using the PBA material nickel hexacyanoferrate (NiHCF), at four different temperatures (15, 35, 55, and 75 °C). Thermodynamic properties, including the intercalation potential (the cathodic peak potential in cyclic voltammetry (CV) scans) and open-circuit potential (OCP), were examined as a function of temperature to characterize the thermal properties of electrode material.[21] Kinetic properties were examined as a function of temperature including the activation energy for charge transfer at the interface between electrode−electrolyte and the activation energy for ion transport in the solid material. An efficient deionization system requires fast interfacial charge transfer with a small activation energy,[22,23] as well as fast ion transport (large diffusion coefficient) with a small activation energy in the solid composite material. A comparison of activation energy of charge transfer and ion transport therefore provides insight into the importance of ion transport in a PBA electrode relative to that of interfacial charge transfer.

EXPERIMENTAL SECTION

Electrode Synthesis. Nickel hexacyanoferrate powders (NiHCF) were produced using a co-precipitation method as previously reported using $Ni(NO_3)_2$ (Sigma-Aldrich, 0.1 M) and $K_3Fe(CN)_6$ (EMD Chemicals, 0.05 M) solutions. These two solutions were added into deionized water with vigorous stirring at room temperature (0.5 mL/min). The precipitates were collected after settling for 1 d, washed by centrifugation for several cycles using DI water, and dried in a vacuum oven (70 °C) for 12 h. The produced NiHCF powders were ground in a mortar and pestle with carbon black (Vulcan XC72R, Cabot, average particle size of 50 nm), poly(vinylidene fluoride) (PVDF, Kynar HSV 900, Arkema, Inc.), and 1-methyl-2-pyrrolidinone (NMP, Sigma-Aldrich) in a mass ratio of 3:1:1. The mixed slurry was drop-cast onto carbon cloth (7 cm^2, 0.356 mm thickness, and 1.5 g/cm^3 density; AvCarb 1071 HCB, AvCarb Material Solutions). Counter electrodes were prepared using activated carbon (AC) instead of NiHCF powders as the active material by the same drop-casting method. The coated samples were dried on a hotplate (70 °C) for 1 h and then heated in a vacuum oven (70 °C) for 12 h.

Material Characterization. Powder X-ray diffraction patterns were recorded using a powder diffractometer (Malvern Panalytical Empyrean) with a Cu Kα (λ_1 = 1.5406 Å, λ_2 = 1.5444 Å) radiation source, at an accelerating voltage of 45 kB and current of 40 mA between 10 and 60° (2θ) with a nominal step size of 0.026°/s. Phase ID was carried out using Jade software from Materials Data, Inc. (MDI). A thermogravimetric analyzer (TGA, NETZSCH STA 449F3, Selb) was used to analyze the thermal stability, dehydration temperature, and water content of each sample under a flowing N_2 gas atmosphere at 25 to 600 °C (10 °C/min) with the sample placed in a crucible (Al_2O_3 85 μL).

Electrochemical Characterization. All electrochemical measurements were carried out with a Biologic VMP3 potentiostat, in three-electrode cells consisting of a NiHCF electrode as the working electrode, AC as the counter electrode, and an Ag/AgCl as the reference electrode (3 M NaCl, +0.209 V with respect to SHE). Before each electrochemical test, the electrodes were immersed in DI water in a vacuum desiccator for 20 min to remove gas bubbles attached to the surface of electrode. Cyclic voltammetry (CV) scans were obtained in different potential windows for each specific ion. All of the presented potentials were corrected for different temperatures using a temperature coefficient of −0.13 mV/°C for the Ag/AgCl reference electrode,[24,25] and the *IR* drop between the working and reference electrodes was obtained from the product of ohmic resistance (R_s) obtained from electrochemical impedance spectroscopy (EIS) and the measured current (I). For example, the corrected potential (E_{cor}) at 55 °C was calculated from the measured potential (E_m) as $E_{cor} = E_m + 0.00013\ V/°C \times (55-25)°C - R_s \times I$. The open-circuit potential (OCP) was recorded using the potentiostat after the temperature stabilized. The state of charge of the electrode at each temperature for each ion was considered to be the same as no pre-charge or pre-discharge process was applied.

Electrochemical impedance spectroscopy (EIS) was conducted over a frequency range of 20 mHz to 500 kHz with an amplitude of 5 mV at the steady-state OCP. All EIS measurements were performed after the electrodes were held at their OCP values for 10 min to achieve steady-state conditions. The ion diffusion coefficient in the solid material (D, cm^2/s) was calculated from EIS results using[26]

$$Z_{Re} = R_s + R_{ct} + \sigma\omega^{-1/2} \quad (1)$$

$$D = \frac{R^2T^2}{2A^2n^4F^4C^2\sigma^2} \quad (2)$$

where σ is the Warburg coefficient associated with Z_{Re}, R is the ideal gas constant (8.314 J/mol·K), T is the absolute temperature (K), A is the geometric surface area of the electrode (cm^2), n is the number of electrons per molecule for the reaction, F is Faraday's constant (96485 C/mol), and C is the ion molar concentration. Solution resistance (R_s, Ω) and interfacial charge transfer resistance (R_{ct}, Ω) are independent of frequency. The intercept of Nyquist plot on Z_{Re} axis was used to determine the R_s, and changes in R_s at different temperatures were used for IR correction in CVs. The high- to medium-frequency semicircle in a Nyquist plot is attributed to the charge transfer at the interface between the electrode and electrolyte, and the straight line in the low-frequency region is caused by ion diffusion into the electrode material.[27] The Warburg coefficient (σ, Ω $s^{1/2}$) was obtained using the generalized Randles equivalent circuit (Supporting Information), which is analogous to the slope of a linear fit between Z_{Re} and the square root of the corresponding angular frequency (ω) in the low-frequency region (Warburg impedance region) by eq 1.[28] R_{ct} was obtained from the semicircle of Nyquist plot with the simple model, which ignored the solid- and liquid-phase resistances within the porous structure of the electrode.[29,30] The calculated D values may reflect properties of the entire porous composite electrode

https://doi.org/10.1021/acs.est.2c01586
Environ. Sci. Technol. 2022, 56, 8932−8941

rather than just diffusion into the active material; therefore, we named D as the ion diffusion coefficient in the solid material.[31] The simplified model provides a general understanding of the intercalation reactions with different monovalent cations.

Galvanostatic charge and discharge tests were conducted for each ion at different temperatures. A constant current of ±7 mA/30 mg (normalized by the mass of active material) was applied in the voltage window based on the redox peaks from CV results. All of the reactors were sealed and wrapped with alumina foil and immersed in a water bath (Precision Microprocessor Controlled 280 Series Water Bath, Thermo Fisher Scientific) set at one of four temperatures (15, 35, 55, and 75 °C). A thermometer was inserted in a control reactor containing only DI water to monitor the temperature inside the reactor. The reactors were held at each temperature for 30 min before obtaining electrochemical data to ensure thermal equilibrium assuming both electrode and electrolyte with the same temperature.

Thermodynamic and Kinetic Analysis. The three most relevant thermodynamic parameters of the electrode reaction are Gibbs energy (G), entropy (S), and enthalpy (H). Cations insertion into NiHCF lattice produces a change in the Gibbs energy (ΔG_i), which equals the difference between the Gibbs energy of the hydrated cation in NiHCF lattice (ΔG_l) and the Gibbs energy of the hydrated cation in the solution (ΔG_s), resulting in the change in cation insertion potential (E_i)[32,33]

$$\Delta G_i = \Delta G_l - \Delta G_s = -nFE_i \tag{3}$$

The change of entropy (ΔS) of cation intercalation and deintercalation can be calculated as a function of the change in the OCP (ΔE, V) with the change in temperature (ΔT, K)[34]

$$\Delta S = nF\frac{\Delta E}{\Delta T} \tag{4}$$

The $\Delta E/\Delta T$ ratio is defined here as the temperature coefficient OCP. A decrease in entropy means that there has been a decrease in the electrode lattice energy due to a more ordered structure.

The overall change in the enthalpy (ΔH) for ion intercalation/deintercalation is[35,36]

$$\Delta H = \Delta G + T\Delta S \tag{5}$$

The heat exchanged (Q_{total}) between the systems and surroundings at constant pressure can be calculated from the heat release due to the current (I) and the change in entropy (ΔS) as[34]

$$Q_{total} = Q_{irev} + Q_{rev} = -I^2R_i - T\Delta S\frac{I}{nF} \tag{6}$$

where I is the current value (the discharge current is determined to be negative), R_i is the internal resistance of the system (cumulative effects of ohmic, activation energy, and diffusion polarization resistances),[34] Q_{irev} is always negative due to the heat loss of current, and Q_{rev} depends on both the current and the change in ΔS. The sum of Q_{irev} and Q_{rev} therefore determines the sign and value of Q_{total}. The contribution of Q_{rev} to Q_{total} is expected to be much higher than 50%, especially at low current rates (lower than 1 C) in ion battery systems.[34]

The exchange-current density (i_0), representing the rate per area of the forward and reverse reactions at equilibrium where the total current is zero, is calculated as[30,37]

$$i_0 = \frac{RT}{nFR_{ct}} \tag{7}$$

where R_{ct} is the interfacial charge transfer resistance (Ω) in eq 1.

The activation energy (E_a, kJ/mol) for the interfacial charge transfer process is the extra energy needed for the ions to move, and it can be calculated from the exchange current (i_0) at different temperatures using[38]

$$i_0 = a\exp\left\{\frac{-E_a}{RT}\right\} \tag{8}$$

Since eqs 7 and 8 are equal to i_0, they can be rearranged so that E_a can be obtained from the slope of a plot of ln (R_{ct}^{-1}) versus $1000/T$ based on the Arrhenius equation[23,39]

$$\ln(R_{ct}^{-1}) = -\frac{E_a}{RT} + b \tag{9}$$

where a and b are constants. The activation energy for ion transport in the solid material, E_a', was calculated using a similar approach based on the Arrhenius equation from the slope of a plot of ln(D) versus $1000/T$ according to[39,40]

$$\ln(D) = -\frac{E_a'}{RT} + b \tag{10}$$

where D (cm^2/s) is the ion diffusion coefficient in the solid material calculated from EIS results using eqs 1 and 2.[26] Ion transport in the lower conductivity materials may include two processes, diffusion driven by the chemical gradients and migration due to the electric potential. However, it is difficult to separate the contributions of these two transport processes in the electrode as both depend on D. Therefore, E_a' is a parameter that quantifies the combined contributions of both diffusion and migration of ion transport in the electrode.

RESULTS AND DISCUSSION

Physicochemical Properties of NiHCF. Powder X-ray diffraction (XRD) patterns for the NiHCF powders showed a typical Prussian blue-type open-framework crystal structure (Figure S1a). The sharp peaks indicated a high crystallinity of the NiHCF powders. Analysis of the XRD data confirmed that the powders had a face-centered cubic phase with a unit cell of 10.201 Å, which closely matched that of the known crystal structure of Prussian blue and its analogues.[41,42] NiHCF powders prepared by the fast co-precipitation process, without the addition of chelators, produced high water contents in the crystal structure (Figure S1b).[43] The weight loss due to surface absorbed water and zeolitic water was ∼22% (at temperatures below 200 °C), and the loss due to coordinated water (200−300 °C) was ∼7%, consistent with previous reports for this preparation process using these materials.[41,44] Taken together, these analysis results confirmed that the NiHCF powders had properties typical of this material.

Thermodynamic Properties Analysis. Multiple processes are included in an electrochemical cell based on porous electrodes of intercalation material. The thermodynamic and kinetic properties of ion adsorption depend on these processes, which include (1) ion transport through the electrolyte-filled porous structure of the electrode, (2) ion intercalation reactions at the electrolyte−solid interface accompanied by charge transfer, (3) ion transport in the solid-phase material, and (4) ion transport in the endplate channel and across the

https://doi.org/10.1021/acs.est.2c01586
Environ. Sci. Technol. 2022, 56, 8932−8941

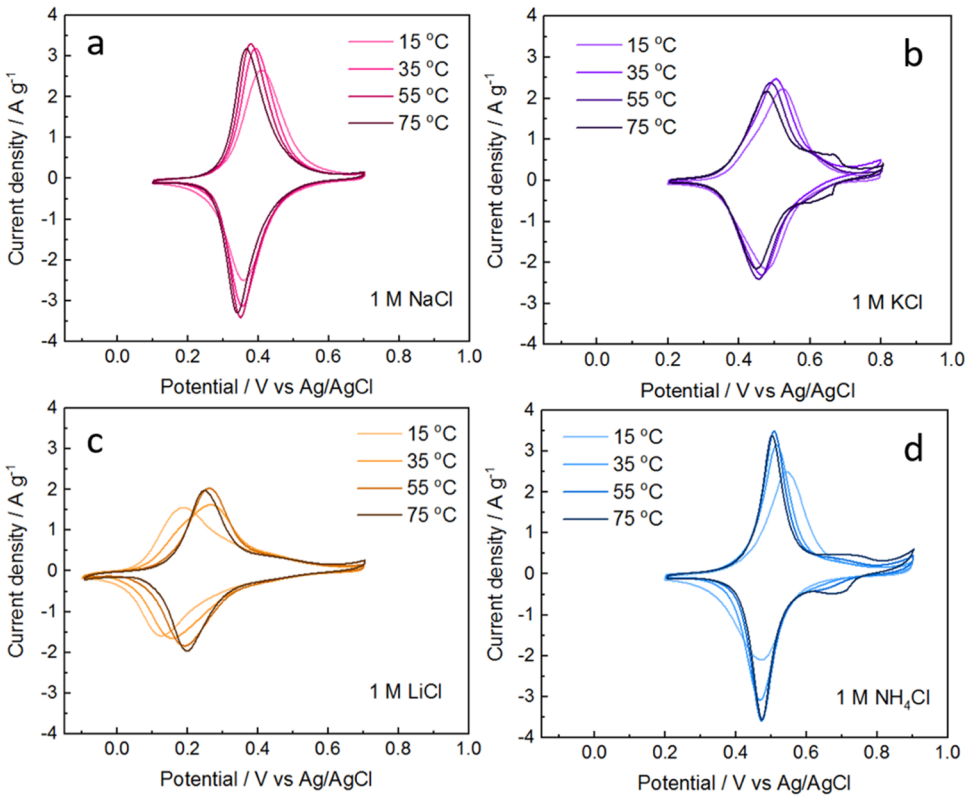

Figure 1. Cyclic voltammetry (CV) of NiHCF electrodes under various temperatures with electrolytes (1 M) for (a) NaCl, (b) KCl, (c) LiCl, and (d) NH_4Cl. The measured potentials were corrected for temperature and the IR between the working and reference electrodes. The scan rate is 2 mV/s.

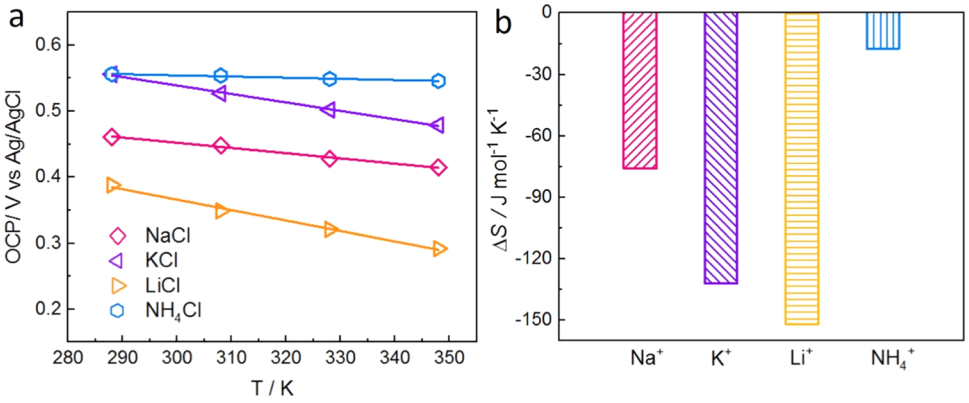

Figure 2. Temperature dependence of the (a) open-circuit potential, and (b) the calculated entropy change for the NiHCF electrodes with four different cations.

ion-exchange membrane.[31,45−48] Our study focused on a single electrode with intercalation material for the transport of multiple monovalent ions. Therefore, only the first three processes were discussed relative to experimental conditions here. Variation in solution temperature produced changes in the thermodynamic properties of the NiHCF electrodes as evidenced by a shift in the half potentials (E_{half}) in CV curves (Table S1), with the response for Li^+ ions different from that of the other ions. Increasing the temperature shifted the reduction (intercalation) potentials (vs Ag/AgCl) to more positive values for Li^+, with a change from 0.125 V (at 15 °C) to 0.198 V (at 75 °C) (Figure 1). This indicated that a higher temperature was beneficial for the intercalation of Li^+. However, for the other ions, increasing the temperature reduced the reduction potentials and shifted them in the opposite direction (to more negative values), which indicated that more energy was required for intercalation with increasing temperature. For oxidation (deintercalation), increasing the temperature shifted the potentials to more negative positions for Na^+, K^+, and NH_4^+, which indicated that higher temperatures were beneficial (less energy required) for the deintercalation of these ions from the electrode. The magnitude of the peak current density increased with temperature from 15 to 55 °C for all four ions, but the peak current density was reduced at the highest temperature of 75 °C. The reduced current density at this highest temperature might be related to a co-ions expulsion effect.[49] At any single temperature, there was an increase (more positive) in

https://doi.org/10.1021/acs.est.2c01586
Environ. Sci. Technol. 2022, 56, 8932−8941

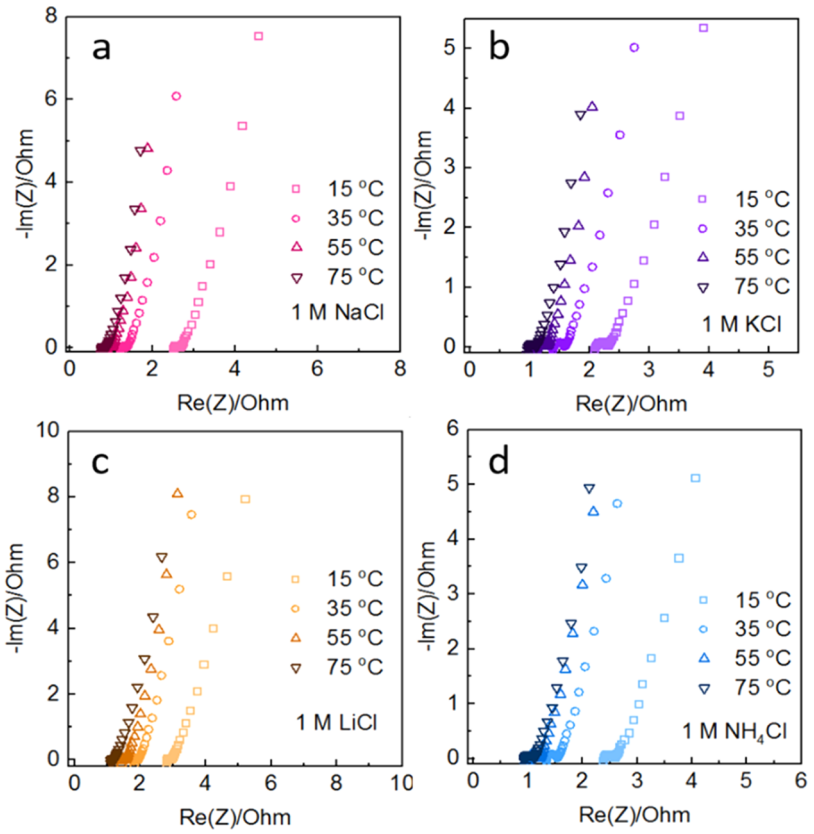

Figure 3. Nyquist plot of NiHCF electrodes under various temperatures with electrolytes of (a) 1 M NaCl, (b) 1 M KCl, (c) 1 M LiCl, and (d) 1 M NH_4Cl. The enlarged figure in the high-frequency region of each figure is presented in Figure S2.

reduction potential (intercalation) for the different ions in the order of Li^+, Na^+, K^+, and NH_4^+ (Figure 1 and Table S1), consistent with the previous reports at room temperature.[41] At 35 °C, for example, the intercalation potentials (vs Ag/AgCl) increased to more positive values in the order 0.156 V for Li^+, 0.354 V for Na^+, 0.461 V for K^+, and 0.469 V for NH_4^+.

The different cathodic peak potentials of each ion, for example, for Li^+ compared to NH_4^+, were due to the change in the Gibbs energy needed for the insertion of these different ions. This change in the Gibbs energy results from the difference in the magnitudes of the energy of the hydrated cation in the crystal lattice after intercalation and the energy of the hydrated cation in solution, or $\Delta G_l - \Delta G_s$ (eq 3).[33] Typically ΔG_l is much smaller than ΔG_s, and therefore, the changes in the intercalation potential of each ion are primarily a function of the magnitude of ΔG_s.[50,51] The intercalation potential decreases inversely with ΔG_s, in the order Li^+ (489 kJ/mol) < Na^+ (383 kJ/mol) < K^+ (312 kJ/mol) < NH_4^+ (301 kJ/mol).[50,52] The shift of reduction (intercalation) and oxidation (deintercalation) potential as temperature increased was therefore larger for the Li^+ with the biggest ΔG_s, resulting in the greater effect of temperature on Li^+ than the other cations.[32]

The reason for a larger shift of anodic than cathodic peaks in CVs as temperature increased (Figure 1) is due to the reversible heat effects in intercalation battery electrodes which are related to the entropy changes.[53] The temperature dependence of the OCP for each ion in the temperature range of 15 to 75 °C was used to calculate free energy components (entropy and enthalpy) (Figure 2a). The increase in temperature resulted in a shift of OCP of all of the four ions to a more negative position, which was consistent with a negative temperature coefficient ($\Delta E/\Delta T$) in the literature for a PBA-based electrode.[54] The $\Delta E/\Delta T$ values obtained from changes in the OCPs (-1.58 ± 0.09 mV/K for Li^+, -0.79 ± 0.05 mV/K for Na^+, -1.37 ± 0.26 mV/K for K^+ and -0.18 ± 0.02 mV/K for NH_4^+) were used to calculate the change in entropy (eq 4), producing $\Delta S = -152$ J/mol·K for Li^+, -76 J/mol·K for Na^+, -132 J/mol·K for K^+, and -17.4 J/mol·K for NH_4^+ (Figure 2b). A negative Q means an exothermic reaction in which heat is transferred from the electrode to the ambient environment (heating effect), while a positive Q means an endothermic reaction in which heat is transferred from the ambient environment to the electrode (cooling effect). As ΔS is always negative for all ions and I is negative in the intercalation (discharge) process (eq 6), $Q_{rev} = -T\Delta SI/nF$ is negative, showing electrode heating. In the deintercalation (charge) process, I and $Q_{rev} = -T\Delta SI/nF$ are positive, resulting in cooling. Therefore, there was a larger shift in the potentials of the anodic peaks in CVs than the cathodic peaks as temperature increased because the higher temperature was beneficial to the deintercalation (endothermic) reaction.[55] The heating or cooling effect (due to the exothermic or endothermic reaction) was stronger for Li^+, Na^+, and K^+ than for NH_4^+ due to their larger absolute values of ΔS.

Kinetic Properties Analysis. The magnitude of the potential of the separation between the oxidation (deintercalation) and reduction (intercalation) peak in the CV tests, or the peak separation (ΔE, V), highly depends on the ion transport in the bulk phase of electrode material and the rate constant at the electrode−electrolyte interface.[23] The peak separation of NiHCF electrode with each ion showed a general

https://doi.org/10.1021/acs.est.2c01586
Environ. Sci. Technol. 2022, 56, 8932−8941

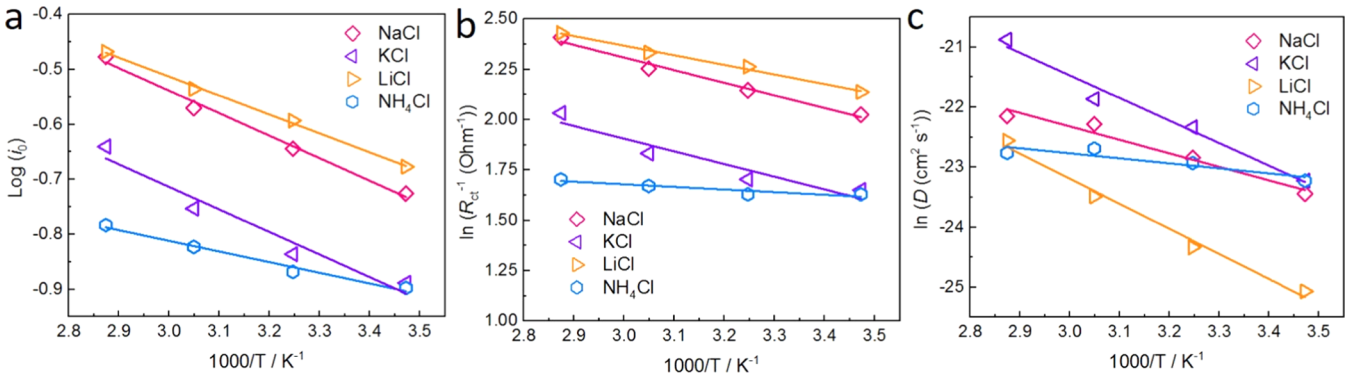

Figure 4. Temperature dependence of plots of (a) $\log(i_0)$ versus 1000/T, (b) $\ln(R_{ct}^{-1})$ versus 1000/T, and (c) $\ln(D)$ versus 1000/T for the NiHCF electrode with 1 M NaCl, KCl, LiCl, and NH_4Cl.

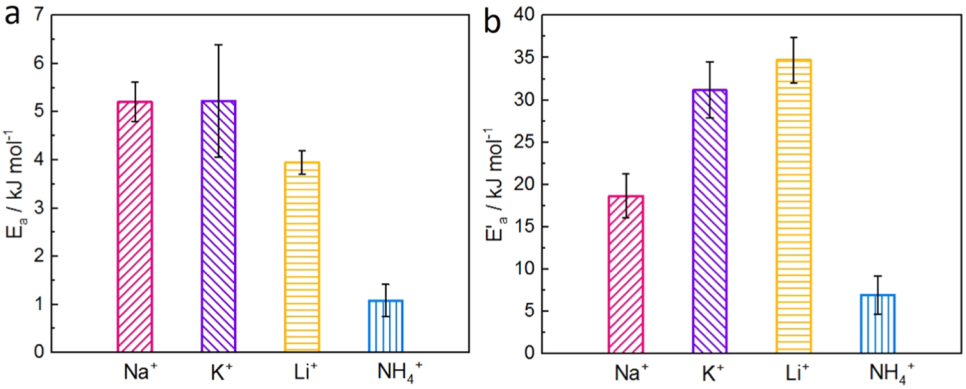

Figure 5. Activation energies for (a) interfacial charge transfer process (E_a) and (b) ion transport process (E_a') for the NiHCF electrode with NaCl, KCl, LiCl, and NH_4Cl.

decreasing trend with increasing temperature (Table S1), which indicated a higher temperature was beneficial for ion transport and/or interfacial transfer of these ions. A larger ΔE for Li^+ at all temperatures (0.049−0.110 V) compared to the other ions (0.025−0.051 V for Na^+, 0.029−0.046 V for K^+, and 0.028−0.070 V for NH_4^+) suggested that transport and/or interfacial transfer of Li^+ was either slower than that of the other ions (Table S1) or there was an additional interfacial reaction such as more water co-intercalation into PBA lattices due to more hydrophilic property of Li^+.[41,56,57]

Charge transfer kinetics were enhanced with increasing temperature as shown by a decrease in charge transfer resistance (R_{ct}) at the interface between electrode and electrolyte, reflected by the decrease in the diameter of the semicircles in high- to medium-frequency region of the Nyquist plot at higher temperature (Figures 3 and S2). The calculated results of exchange-current density (i_0) (Table S2) as a function of temperature (T) using eq 7 showed a positive correlation between i_0 and T and good agreement with the predicted linear relationship between the logarithm of i_0 and T^{-1} (Figure 4a). The linear correlation obtained between $\ln(R_{ct}^{-1})$ and 1000/T (Figure 4b) further supported the use of an Arrhenius equation for calculating activation energy E_a (eqs 8 and 9).[23,39] The activation energy E_a at the electrode−electrolyte interface was small for all ions (3.9 ± 0.2 kJ/mol for Li^+, 5.2 ± 0.4 kJ/mol for Na^+, 5.2 ± 1.2 kJ/mol for K^+, and 1.1 ± 0.3 kJ/mol for NH_4^+), indicating high rates of interfacial charge transfer (Figure 5a), which was consistent with the reported values in the literature (E_a of 5.1 ± 0.4 in $NaNO_3$ aqueous solution for a NiHCF electrode).[23] Small activation energies were consistent with the previous results that PBA electrodes could intercalate and deintercalate hydrated or partially hydrated ions rather than requiring bare alkali ions.[23] For example, the radius of hydrated Na^+ (3.6 Å), hydrated K^+ (3.3 Å), and hydrated NH_4^+ (3.3 Å) are close to the interstitial sites of PBA material (3.2−4.6 Å).[58−60] Therefore, the interfacial charge transfer of these ions does not require full ion dehydration, and therefore the transfer of partially hydrated ions could have contributed to the fast charge transfer process. However, the much larger hydrated radius Li^+ (3.8 Å) may require a larger degree of dehydration which would account for its lowest intercalation potential in the CVs (Figure 1).[32,33] It should be noted that the charge transfer resistance is highly dependent on electrode potential, which can be further described by the combination of the Frumkin isotherm with the Butler−Volmer equation.[31,48,61,62]

Ion transport kinetics in the solid phase of the NiHCF electrodes increased for each ion with temperature as shown by the increased ion diffusion coefficient (D) calculated by the Warburg element (Warburg coefficient σ, Figure S3, Table S2, eqs 1 and 2). The calculated D value matched well with the literature, which was reported to be proportional to the electronic conductivity of nanoparticle agglomerates on the electrode, and the path length for diffusion was dependent on the size of nanoparticle agglomerates.[47,63] The good linear correlation between $\ln(D)$ as a function of 1000/T (Figure 4c) supported the use of this form of the Arrhenius equation (eq 10).[23,39] These results indicated that D can be described as the thermal activation process with the activation energy for ion transport in the solid material. The activation energy for ion

https://doi.org/10.1021/acs.est.2c01586
Environ. Sci. Technol. 2022, 56, 8932−8941

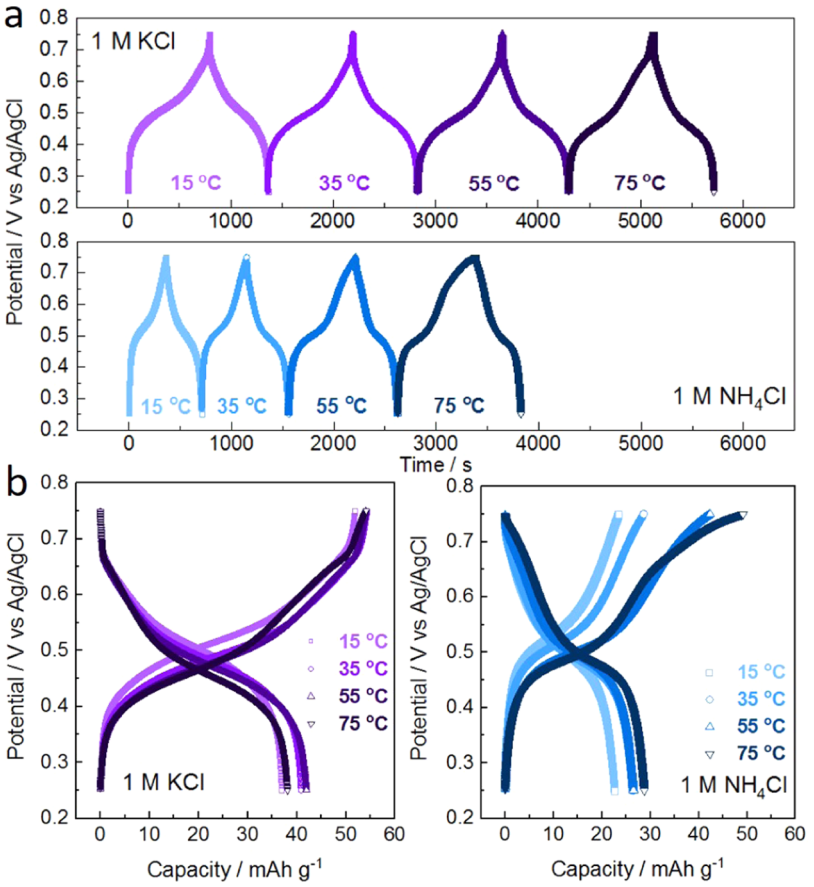

Figure 6. Galvanostatic charge and discharge profiles of NiHCF electrode under various temperatures with electrolytes of 1 M KCl and NH_4Cl at ± 7 mA/30 mg: (a) potential vs time and (b) potential vs capacity profiles.

transport (E_a') equals the value of the energy barrier that has to be overcome by the atom to take a new balanced position in the neighboring node or internode.[40,64] E_a' values for ion transport in the solid material (35 ± 3 kJ/mol for Li^+, 19 ± 2 kJ/mol for Na^+, 31 ± 3 kJ/mol for K^+, and 7 ± 2 kJ/mol for NH_4^+) were much larger than those for interfacial charge transfer (Figure 5b). The greater activation energies indicated that the ion transport in the solid phase of the NiHCF electrode was the rate-controlling step. Our findings were consistent with previous reports on modeling ion transport in porous intercalation electrodes that ion transport, both in the porous structure and solid phase of the electrode, is rate-limiting rather than the charge transfer processes between the electrolyte and the intercalation material.[31,45,48,65] Since Li^+ has the smallest diffusion coefficient (Table S2) of the four ions examined here, this property likely explains why it had the largest ΔE in CVs of the four different ions at any single temperature (Figure 1).

The effect of temperature on ion adsorption capacity was examined for the cations with the large activation energy (K^+), the small activation energy (NH_4^+), and the most abundant cation in seawater (Na^+) (Figures 6 and S4). The ion adsorption (discharge) capacity for NH_4^+ increased by 28.1% from 15 to 75 °C (22.4−28.7 mAh/g). For K^+ and Na^+, there was no continuous increase in capacity with temperature. For K^+, there was a 12.6% increase in capacity between 15 and 55 °C (37.1−41.8 mAh/g) but at 75 °C, the capacity (38.1 mAh/g) decreased so that it was only 2.7% larger than that at 15 °C. Similarly, for Na^+, the capacity increased by 7.5% between 15 and 35 °C (42.7−45.9 mAh/g), but it decreased at 75 °C (43.3 mAh/g) (Figure S4). The Li^+ galvanostatic charge and discharge profiles were not included here as the intercalation and deintercalation process likely requires multiple dehydration and rehydration steps due to its much larger hydrated radius (3.8 Å) than the other hydrated ions relative to the sizes of interstitial sites.[33,66] These results suggested that charge and discharge capacities were less impacted by temperature for ions with bigger activation energies (both interfacial charge transfer and the ion transport in solid material), such as K^+ and Na^+, than those with smaller activation energies like NH_4^+. Therefore, increased temperatures can be used to best enhance ions with smaller activation energies. At intercalation equilibrium, a relationship of intercalation degree with electrode potential can be further simulated by the Frumkin isotherm model.[30,31,46]

Outlook. The thermodynamic and kinetic behavior of NiHCF electrodes as a function of temperature is examined for four different monovalent cations, which is important for ion-selective electrode development.[67] From the thermodynamic analysis, as the temperature increased, the intercalation potential of the ion with higher hydrated energies shifted more than the ions with lower hydrated energies. The temperature impacted the charge cycle differently from that of the discharge cycle. Lower temperatures favored discharge of the electrodes (intercalation) as it was an exothermic reaction, while higher temperatures improved the charge step (deintercalation) as it was an endothermic reaction. However, from the kinetic analysis, a higher operating temperature was

https://doi.org/10.1021/acs.est.2c01586
Environ. Sci. Technol. 2022, 56, 8932−8941

beneficial for both charge transfer at the interface between electrode and electrolyte, as well as ion transport in the solid material. The larger activation energy for ion transport in the solid phase of NiHCF electrode (E_a') than the activation energy for interfacial charger transfer (E_a) indicated that ion transport in the solid phase of NiHCF electrodes was the rate-controlling step for all of these cations during intercalation and deintercalation process. As a result, the charge and discharge capacities were improved more for ions with smaller activation energies (such as NH_4^+) with an increase in the operating temperature compared to the ions with larger activation energies. Using EIS measurements to analyze complex electrode processes has always been an active research topic for understanding ion transport and reaction kinetics. There is room to extend the model used in this study to infer more accurate and resolved kinetic parameters, but the goal here to understand monovalent cation transport can be ascertained with the current simplified model. Future efforts to examine ion transport could improve the resolution of diffusion in different electrode regions, and identification of material electrical resistance. The findings from this work indicate that active materials with smaller sizes would provide better performance as the diffusion time in the solid phase will be increased if larger particle sizes were used. Also, the thermodynamic and kinetic values of ions studied here were in a supporting electrolyte (1 M) more concentrated than in typical BDI experiments (<0.1 M), which would need careful attention on direct comparisons with values obtained under different ion concentrations.

■ ASSOCIATED CONTENT

Supporting Information

The Supporting Information is available free of charge at https://pubs.acs.org/doi/10.1021/acs.est.2c01586.

Powder X-ray diffraction (XRD) spectra and thermogravimetric analysis (TGA) of NiHCF powders, Nyquist plots in the high-frequency region, equivalent circuit, and galvanostatic charge and discharge profiles of the NiHCF electrode (PDF)

■ AUTHOR INFORMATION

Corresponding Author

Bruce E. Logan − *Department of Civil and Environmental Engineering, The Pennsylvania State University, University Park, Pennsylvania 16802, United States;* orcid.org/0000-0001-7478-8070; Phone: +1-814-863-7908; Email: blogan@psu.edu

Authors

Le Shi − *Department of Civil and Environmental Engineering, The Pennsylvania State University, University Park, Pennsylvania 16802, United States;* orcid.org/0000-0003-1794-1256

Xiangyu Bi − *Department of Civil and Environmental Engineering, The Pennsylvania State University, University Park, Pennsylvania 16802, United States;* orcid.org/0000-0003-2706-3039

Evan Newcomer − *Department of Civil and Environmental Engineering, The Pennsylvania State University, University Park, Pennsylvania 16802, United States*

Derek M. Hall − *Department of Energy and Mineral Engineering, The Pennsylvania State University, University Park, Pennsylvania 16802, United States;* orcid.org/0000-0001-9648-596X

Christopher A. Gorski − *Department of Civil and Environmental Engineering, The Pennsylvania State University, University Park, Pennsylvania 16802, United States;* orcid.org/0000-0002-5363-2904

Complete contact information is available at: https://pubs.acs.org/10.1021/acs.est.2c01586

Notes

The authors declare no competing financial interest.

■ ACKNOWLEDGMENTS

Funding for data presented here was provided by the USAID and NAS through Subaward 2000010557 (BEL), and any opinions, findings, conclusions, or recommendations expressed here are those of the authors alone and do not necessarily reflect the views of USAID or NAS.

■ REFERENCES

(1) Suss, M. E.; Presser, V. Water desalination with energy storage electrode materials. *Joule* **2018**, *2*, 10−15.

(2) Wang, L.; Dykstra, J. E.; Lin, S. Energy efficiency of capacitive deionization. *Environ. Sci. Technol.* **2019**, *53*, 3366−3378.

(3) Porada, S.; Zhao, R.; van der Wal, A.; Presser, V.; Biesheuvel, P. M. Review on the science and technology of water desalination by capacitive deionization. *Prog. Mater. Sci.* **2013**, *58*, 1388−1442.

(4) Zhang, X.; Zuo, K.; Zhang, X.; Zhang, C.; Liang, P. Selective ion separation by capacitive deionization (cdi) based technologies: A state-of-the-art review. *Environ. Sci.: Water Res. Technol.* **2020**, *6*, 243−257.

(5) Kim, T.; Gorski, C. A.; Logan, B. E. Low energy desalination using battery electrode deionization. *Environ. Sci. Technol. Lett.* **2017**, *4*, 444−449.

(6) Zhang, C.; Ma, J.; Wu, L.; Sun, J.; Wang, L.; Li, T.; Waite, T. D. Flow electrode capacitive deionization (fcdi): Recent developments, environmental applications, and future perspectives. *Environ. Sci. Technol.* **2021**, *55*, 4243−4267.

(7) Shi, W.; Zhou, X.; Li, J.; Meshot, E. R.; Taylor, A. D.; Hu, S.; Kim, J.-H.; Elimelech, M.; Plata, D. L. High-performance capacitive deionization via manganese oxide-coated, vertically aligned carbon nanotubes. *Environ. Sci. Technol. Lett.* **2018**, *5*, 692−700.

(8) Shi, L.; Bi, X.; Newcomer, E.; Hall, D. M.; Gorski, C. A.; Galal, A.; Logan, B. E. Co-precipitation synthesis control for sodium ion adsorption capacity and cycle life of copper hexacyanoferrate electrodes in battery electrode deionization. *Chem. Eng. J.* **2022**, *435*, No. 135001.

(9) Wang, K.; Zhang, H.; Chen, G.; Tian, T.; Tao, K.; Liang, L.; Gao, J.; Cao, H. Long-term-stable wo3-pb complementary electrochromic devices. *J. Alloys Compd.* **2021**, *861*, No. 158534.

(10) Son, M.; Shim, J.; Park, S.; Yoon, N.; Jeong, K.; Cho, K. H. Seawater battery desalination with sodium-intercalation cathode for hypersaline water treatment. *Desalination* **2022**, *531*, No. 115713.

(11) Qu, Y.; Campbell, P. G.; Gu, L.; Knipe, J. M.; Dzenitis, E.; Santiago, J. G.; Stadermann, M. Energy consumption analysis of constant voltage and constant current operations in capacitive deionization. *Desalination* **2016**, *400*, 18−24.

(12) Son, M.; Pothanamkandathil, V.; Yang, W.; Vrouwenvelder, J. S.; Gorski, C. A.; Logan, B. E. Improving the thermodynamic energy efficiency of battery electrode deionization using flow-through electrodes. *Environ. Sci. Technol.* **2020**, *54*, 3628−3635.

(13) Park, S.; Ligaray, M.; Kim, Y.; Chon, K.; Son, M.; Cho, K. H. Investigating the influence of catholyte salinity on seawater battery desalination. *Desalination* **2021**, *506*, No. 115018.

(14) Shi, L.; Newcomer, E.; Son, M.; Pothanamkandathil, V.; Gorski, C. A.; Galal, A.; Logan, B. E. Metal-ion depletion impacts the stability

and performance of battery electrode deionization over multiple cycles. *Environ. Sci. Technol.* **2021**, *55*, 5412−5421.
(15) Zhang, J.; Hatzell, K. B.; Hatzell, M. C. A combined heat- and power-driven membrane capacitive deionization system. *Environ. Sci. Technol. Lett.* **2017**, *4*, 470−474.
(16) Moreno, D.; Hatzell, M. C. Efficiency of thermally assisted capacitive mixing and deionization systems. *ACS Sustainable Chem. Eng.* **2019**, *7*, 11334−11340.
(17) Huang, K. Z.; Tang, H. L. Temperature and desorption mode matter in capacitive deionization process for water desalination. *Environ. Technol.* **2020**, *41*, 3456−3463.
(18) Ma, P.; Sun, Y.; Zhang, X.; Chen, J.; Yang, B.; Zhang, Q.; Gao, X.; Yan, X. Spinel-type solar-thermal conversion coatings on supercapacitors: An effective strategy for capacitance recovery at low temperatures. *Energy Storage Mater.* **2019**, *23*, 159−167.
(19) Yi, F.; Ren, H.; Dai, K.; Wang, X.; Han, Y.; Wang, K.; Li, K.; Guan, B.; Wang, J.; Tang, M.; Shan, J.; Yang, H.; Zheng, M.; You, Z.; Wei, D.; Liu, Z. Solar thermal-driven capacitance enhancement of supercapacitors. *Energy Environ. Sci.* **2018**, *11*, 2016−2024.
(20) Lu, Y.; Xu, J.; Zhao, C.; Gao, Z.; Song, Y.-Y. Boosting the local temperature of hybrid prussian blue/nio nanotubes by solar light: Effect on energy storage. *ACS Sustainable Chem. Eng.* **2021**, *9*, 11837−11846.
(21) Mao, J.; Zhang, P.; Liu, X.; Liu, Y.; Shao, G.; Dai, K. Entropy change characteristics of the lini0.5mn1.5o4 cathode material for lithium-ion batteries. *ACS Omega* **2020**, *5*, 4109−4114.
(22) Mizuno, Y.; Okubo, M.; Asakura, D.; Saito, T.; Hosono, E.; Saito, Y.; Oh-ishi, K.; Kudo, T.; Zhou, H. Impedance spectroscopic study on interfacial ion transfers in cyanide-bridged coordination polymer electrode with organic electrolyte. *Electrochim. Acta* **2012**, *63*, 139−145.
(23) Mizuno, Y.; Okubo, M.; Hosono, E.; Kudo, T.; Zhou, H.; Oh-ishi, K. Suppressed activation energy for interfacial charge transfer of a prussian blue analog thin film electrode with hydrated ions (li+, na+, and Mg2+). *J. Phys. Chem. C* **2013**, *117*, 10877−10882.
(24) Ansuini, F. J.; Dimond, J. R. Factors affecting the accuracy of reference electrodes. *Mater. Perform.* **1994**, *33*, 14−17.
(25) Hall, D. M.; Beck, J. R.; Brand, E.; Ziomek-Moroz, M.; Lvov, S. N. Copper-copper sulfate reference electrode for operating in high temperature and high pressure aqueous environments. *Electrochim. Acta* **2016**, *221*, 96−106.
(26) Ren, W.; Qin, M.; Zhu, Z.; Yan, M.; Li, Q.; Zhang, L.; Liu, D.; Mai, L. Activation of sodium storage sites in prussian blue analogues via surface etching. *Nano Lett.* **2017**, *17*, 4713−4718.
(27) Mathis, T. S.; Kurra, N.; Wang, X.; Pinto, D.; Simon, P.; Gogotsi, Y. Energy storage data reporting in perspective—guidelines for interpreting the performance of electrochemical energy storage systems. *Adv. Energy Mater.* **2019**, *9*, No. 1902007.
(28) Ho, C.; Raistrick, I. D.; Huggins, R. A. Application of a-c techniques to the study of lithium diffusion in tungsten trioxide thin films. *J. Electrochem. Soc.* **1980**, *127*, 343−350.
(29) Suss, M. E.; Baumann, T. F.; Worsley, M. A.; Rose, K. A.; Jaramillo, T. F.; Stadermann, M.; Santiago, J. G. Impedance-based study of capacitive porous carbon electrodes with hierarchical and bimodal porosity. *J. Power Sources* **2013**, *241*, 266−273.
(30) He, F.; Bazant, M. Z.; Hatton, T. A. Equivalent circuit model for electrosorption with redox active materials*arXiv preprint arXiv:2101.00091* 2020 https://arxiv.org/abs/2101.00091.
(31) Levi, M. D.; Aurbach, D. Frumkin intercalation isotherm — a tool for the description of lithium insertion into host materials: A review. *Electrochim. Acta* **1999**, *45*, 167−185.
(32) Scholz, F.; Dostal, A. The formal potentials of solid metal hexacyanometalates. *Angew. Chem., Int. Ed.* **1996**, *34*, 2685−2687.
(33) Lee, H.-W.; Pasta, M.; Wang, R. Y.; Ruffo, R.; Cui, Y. Effect of the alkali insertion ion on the electrochemical properties of nickel hexacyanoferrate electrodes. *Faraday Discuss.* **2014**, *176*, 69−81.
(34) Shi, W.; Zheng, J.; Xiao, J.; Chen, X.; Polzin, B. J.; Zhang, J.-G. The effect of entropy and enthalpy changes on the thermal behavior of li-mn-rich layered composite cathode materials. *J. Electrochem. Soc.* **2016**, *163*, A571−A577.
(35) Bard, A. J.; Faulkner, L. R. *Electrochemical methods: Fundamentals and applications.* 2001, 49.
(36) Thomas, K. E.; Bogatu, C.; Newman, J. Measurement of the entropy of reaction as a function of state of charge in doped and undoped lithium manganese oxide. *J. Electrochem. Soc.* **2001**, *148*, A570.
(37) Zhou, X.; Zou, Y.; Yang, J. Carbon supported tin-based nanocomposites as anodes for li-ion batteries. *J. Solid State Chem.* **2013**, *198*, 231−237.
(38) Fuller, T. F.; Harb, J. N. *Electrochemical engineering.*, John Wiley & Sons, 2018; p 47.
(39) Lin, Z.; Shi, H.-Y.; Lin, L.; Yang, X.; Wu, W.; Sun, X. A high capacity small molecule quinone cathode for rechargeable aqueous zinc-organic batteries. *Nat. Commun.* **2021**, *12*, No. 4424.
(40) Askeland, D. R. *The science and engineering of materials.* 1996, 120.
(41) Wessells, C. D.; Peddada, S. V.; McDowell, M. T.; Huggins, R. A.; Cui, Y. The effect of insertion species on nanostructured open framework hexacyanoferrate battery electrodes. *J. Electrochem. Soc.* **2011**, *159*, A98−A103.
(42) Wessells, C. D.; Peddada, S. V.; Huggins, R. A.; Cui, Y. Nickel hexacyanoferrate nanoparticle electrodes for aqueous sodium and potassium ion batteries. *Nano Lett.* **2011**, *11*, 5421−5425.
(43) Li, W.-J.; Han, C.; Cheng, G.; Chou, S.-L.; Liu, H.-K.; Dou, S.-X. Chemical properties, structural properties, and energy storage applications of prussian blue analogues. *Small* **2019**, *15*, No. 1900470.
(44) Hurlbutt, K.; Wheeler, S.; Capone, I.; Pasta, M. Prussian blue analogs as battery materials. *Joule* **2018**, *2*, 1950−1960.
(45) Singh, K.; Bouwmeester, H. J. M.; de Smet, L. C. P. M.; Bazant, M. Z.; Biesheuvel, P. M. Theory of water desalination with intercalation materials. *Phys. Rev. Appl.* **2018**, *9*, No. 064036.
(46) Porada, S.; Shrivastava, A.; Bukowska, P.; Biesheuvel, P. M.; Smith, K. C. Nickel hexacyanoferrate electrodes for continuous cation intercalation desalination of brackish water. *Electrochim. Acta* **2017**, *255*, 369−378.
(47) Levi, M. D.; Aurbach, D. Simultaneous measurements and modeling of the electrochemical impedance and the cyclic voltammetric characteristics of graphite electrodes doped with lithium. *J. Phys. Chem. B* **1997**, *101*, 4630−4640.
(48) Jung, S. Y.; Joo, H.; Kim, J. H.; Kim, S.; Heo, S.; Yoon, J. Electrode design and performance of flow-type electrochemical lithium recovery (elr) systems. *Desalination* **2022**, *532*, No. 115732.
(49) Biesheuvel, P. M.; van der Wal, A. Membrane capacitive deionization. *J. Membr. Sci.* **2010**, *346*, 256−262.
(50) Marcus, Y. Thermodynamics of solvation of ions. Part 5.—gibbs free energy of hydration at 298.15 k. *J. Chem. Soc., Faraday Trans.* **1991**, *87*, 2995−2999.
(51) Pournaghi-Azar, M. H.; Nahalparvari, H. Electroless preparation and electrochemical behavior of a platinum-doped nickel hexacyanoferrate film−zinc modified electrode: Catalytic ability of the electrode for electrooxidation of methanol. *J. Solid State Electrochem.* **2004**, *8*, 550−557.
(52) Marcus, Y. *Ions in Solution and their Solvation.*, John Wiley & Sons, 2015.
(53) Gunnarshaug, A. F.; Vie, P. J. S.; Kjelstrup, S. Review—reversible heat effects in cells relevant for lithium-ion batteries. *J. Electrochem. Soc.* **2021**, *168*, No. 050522.
(54) Lee, S. W.; Yang, Y.; Lee, H.-W.; Ghasemi, H.; Kraemer, D.; Chen, G.; Cui, Y. An electrochemical system for efficiently harvesting low-grade heat energy. *Nat. Commun.* **2014**, *5*, No. 3942.
(55) Maeda, Y. Thermal behavior on graphite due to electrochemical intercalation. *J. Electrochem. Soc.* **1990**, *137*, 3047−3052.
(56) Liu, S.; Smith, K. C. Effects of interstitial water and alkali cations on the expansion, intercalation potential, and orbital coupling of nickel hexacyanoferrate from first principles. *J. Appl. Phys.* **2022**, *131*, No. 105101.

https://doi.org/10.1021/acs.est.2c01586
Environ. Sci. Technol. 2022, 56, 8932−8941

(57) Fang, Z.; Yin, Y.; Qiu, X.; Zhu, L.; Dong, X.; Wang, Y.; Xia, Y. Prussian blue cathode with intercalation pseudocapacitive behavior for low-temperature batteries. *Adv. Energy Sustainability Res.* **2021**, *2*, No. 2100105.
(58) Israelachvili, J. N. 4 - Interactions Involving Polar Molecules. In *Intermolecular and Surface Forces*, 3rd ed.; Israelachvili, J. N., Ed.; Academic Press: San Diego, 2011; pp 71−90.
(59) Wang, R. Y.; Shyam, B.; Stone, K. H.; Weker, J. N.; Pasta, M.; Lee, H.-W.; Toney, M. F.; Cui, Y. Reversible multivalent (monovalent, divalent, trivalent) ion insertion in open framework materials. *Adv. Energy Mater.* **2015**, *5*, No. 1401869.
(60) Nightingale, E. R. Phenomenological theory of ion solvation. Effective radii of hydrated ions. *J. Phys. Chem. A* **1959**, *63*, 1381−1387.
(61) Levi, M. D.; Salitra, G.; Markovsky, B.; Teller, H.; Aurbach, D.; Heider, U.; Heider, L. Solid-state electrochemical kinetics of li-ion intercalation into li1− x coo2: Simultaneous application of electroanalytical techniques sscv, pitt, and eis. *J. Electrochem. Soc.* **1999**, *146*, 1279.
(62) Smith, K. C.; Dmello, R. Na-ion desalination (nid) enabled by na-blocking membranes and symmetric na-intercalation: Porous-electrode modeling. *J. Electrochem. Soc.* **2016**, *163*, A530.
(63) Shrivastava, A.; Smith, K. C. Electron conduction in nanoparticle agglomerates limits apparent na+ diffusion in prussian blue analogue porous electrodes. *J. Electrochem. Soc.* **2018**, *165*, A1777.
(64) Askeland, D. R., The science and engineering of materials.
(65) West, K.; Jacobsen, T.; Atlung, S. Modeling of porous insertion electrodes with liquid electrolyte. *J. Electrochem. Soc.* **1982**, *129*, 1480−1485.
(66) Gaddam, R. R.; Katzenmeier, L.; Lamprecht, X.; Bandarenka, A. S. Review on physical impedance models in modern battery research. *Phys. Chem. Chem. Phys.* **2021**, *23*, 12926−12944.
(67) Bo, Z.; Huang, Z.; Xu, C.; Chen, Y.; Wu, E.; Yan, J.; Cen, K.; Yang, H.; Ostrikov, K. Anion-kinetics-selective graphene anode and cation-energy-selective MXene cathode for high-performance capacitive deionization. *Energy Storage Materials* **2022**, *50*, 395−406.

Recommended by ACS

Sustainable Underwater Solar Conversion Systems with Enhanced Electrode Environmental Compatibility
Qi Dang, Liang Tang, *et al.*
JANUARY 03, 2022
ACS SUSTAINABLE CHEMISTRY & ENGINEERING
READ

Insight into Electrochemical Properties and Reaction Mechanism of a Cobalt-Rich Prussian Blue Analogue Cathode in a $NaSO_3CF_3$ Electrolyte for Aqueous Sod...
Dongxue Luo, Xingde Xiang, *et al.*
FEBRUARY 26, 2020
THE JOURNAL OF PHYSICAL CHEMISTRY C
READ

Organic Solvothermal Method Promoted Monoclinic Prussian Blue as a Superior Cathode for Na-Ion Batteries
Shiqi Wang, Ya You, *et al.*
APRIL 28, 2022
ACS APPLIED ENERGY MATERIALS
READ

Metal-Ion Depletion Impacts the Stability and Performance of Battery Electrode Deionization over Multiple Cycles
Le Shi, Bruce E. Logan, *et al.*
MARCH 30, 2021
ENVIRONMENTAL SCIENCE & TECHNOLOGY
READ

Get More Suggestions >

https://doi.org/10.1021/acs.est.2c01586
Environ. Sci. Technol. 2022, 56, 8932−8941